nature communications

Article

https://doi.org/10.1038/s41467-025-60170-0

The geometric-electronic coupled design of diatomic catalyst towards oxygen reduction reaction

Received: 6 January 2025

Accepted: 15 May 2025

Published online: 03 June 2025

Check for updates

Yan Liu[1,5], Yan Yang[1,5], Xuanni Lin[2,5], Yutao Lin[1], Zhiwen Zhuo[3] ✉, Dong Liu[2] ✉, Junjie Mao[1] ✉ & Jun Jiang[4] ✉

Diatomic catalysts are promising candidates for heterogeneous catalysis, whereas the rational design meets the challenges of numerous optional elements and the correlated alternation of parameters that affect the performance. Herein, we demonstrate a geometric-electronic coupled design of diatomic catalysts towards oxygen reduction reaction through machine learning derived catalytic "hot spot map". The hot spot map is constructed with two descriptors as axes, including the geometric distance of the diatom and electronic magnetic moment. The narrow hot region in the map indicates the necessary collaborative regulation of the geometric and electronic effects for catalyst design. As a predicted ideal catalyst for oxygen reduction reaction, the N-bridged Co, Mn diatomic catalyst (Co-N-Mn/NC) is experimentally synthesized with a half-wave potential of 0.90 V, together with the embodied zinc air battery displaying high peak power density of 271 mW cm^{-2} and specific capacity of 806 mAh g^{-1}_{Zn}. This work presents an advanced prototype for the comprehensive design of catalysts.

Engineering catalysts at the atomic level leads to the development of modern heterogeneous catalysis and boosts the discovery of single-atom catalysis[1]. In recent years, neighboring two single atoms into diatomic catalysts has provided a powerful means to further tailor the catalytic properties based on the atomically synergistic effect[2–4]. Compared with the limited metal center for single-atom catalysts, the quantity of the selection of metal species for diatomic catalysts exhibits a growth in the square order, significantly broadening the family of single-atom catalysis[5]. However, the numerous optional elements of diatomic catalysts severely increase the time cost of traditional trial-and-error approach for the screening of single-atom catalysts[6,7].

To substitute the trial-and-error approach by the purposeful design of diatomic catalysts, it is desired to identify the most important catalysis-related parameters from the numerous structural factors of diatomic catalysts, such as bond length, d-band center, etc[8–12]. According to the principles of catalytic action, these parameters include the geometric factors and the electronic factors. For example, a volcano-shaped curve correlation between site distance and catalytic activity was discovered in dual-site catalysts through the manipulation of the spacing between heterogeneous synergistic catalytic sites[13]. As another example, Chen and co-workers constructed an asymmetric nitrogen, sulfur-coordinated diatomic iron catalyst, breaking the symmetrical electron distribution of Fe-N_4 moiety and optimizing the adsorption of oxygen-containing intermediates, thereby enhancing the overall catalytic performance[14]. Despite the current progress in manipulating geometric or electronic effects, the geometric parameters and electronic parameters are commonly highly correlated in the system of diatomic catalysts[15–18]. Accordingly, one-sided

[1]School of Chemistry and Materials Science, Anhui Normal University, Wuhu 241002, PR China. [2]State Key Laboratory of Organic-Inorganic Composites, College of Chemical Engineering, Beijing University of Chemical Technology, Beijing 100029, PR China. [3]Hefei National Research Center for Physical Sciences at the Microscale, University of Science and Technology of China, Hefei 230026, PR China. [4]Key Laboratory of Precision and Intelligent Chemistry, School of Chemistry and Materials Science, University of Science and Technology of China, Hefei 230026, PR China. [5]These authors contributed equally: Yan Liu, Yan Yang, Xuanni Lin. ✉e-mail: zhuozw@ustc.edu.cn; liudong@mail.buct.edu.cn; maochem@ahnu.edu.cn; jiangj1@ustc.edu.cn

optimization of either geometric or electronic structure for diatomic catalysts commonly encounters the challenge of unfavorable coupled alternation, leaving difficulty in the rational design.

Considering the strong ability of machine learning (ML) on the mechanistic study in complicated catalysis, we herein constructed a geometric-electronic coupled design of diatomic catalyst derived by ML. Taking electrocatalytic oxygen reduction reaction (ORR) as the model reaction, we analyzed the influence of geometric and electronic parameters on ORR catalysts by ML, demonstrating a coupled design principle via a catalytic "hot spot map". When the active center atom was validated, the geometric distance descriptor of the diatom and electronic magnetic moment descriptor constituted the two axes of the hot spot map. In the hot spot map, the predicted ideal ORR catalysts were located in a narrow region that required the collaborative regulation of the distance between two metal atoms and the magnetic moment of the active center metal atoms. Based on the geometric-electronic coupled design, we predicted Co-N-Mn/NC as an ideal ORR catalyst and verified the effectiveness by experimental study. In alkaline electrolyte, the synthesized Co-N-Mn/NC catalyst exhibited a half-wave potential ($E_{1/2}$) of 0.90 V and a kinetic current density (J_k) of 48.64 mA cm^{-2} at 0.85 V, significantly higher than those of commercial Pt/C. Furthermore, the zinc air battery (ZAB) with Co-N-Mn/NC catalyst achieved remarkable peak power density of 271 mW cm^{-2} and specific capacity of 806 mAh g^{-1}_{Zn}.

Results

Design framework for diatomic ORR catalyst

As illustrated in Fig. 1, we developed a comprehensive workflow to construct a principle coupling of both geometric and electronic effects for the design of diatomic ORR catalysts, which integrates DFT calculation and ML. Moreover, the screened diatomic ORR catalyst was verified by experimental synthesis and corresponding catalytic performance. For the convenience of the experimental synthesis, we chose transition metal-anchored nitrogen-coordinated carbon substrates for diatomic catalysts with M_1-N-M_2/NC (M_2N_7-C) structure, which was explored for other electrocatalysis[19–22]. Additionally, through sharing a bridge N atom between two separate MN_4 moieties, this diatom possessed the moderate atomic distance to ensure interaction between the two moieties with a validated active center. Initially, we divided the features of this system into geometric parameters, electronic parameters, and systematic parameters to theoretically decouple the geometric and electronic effects. Subsequently, we employed the DFT calculations to obtain the database as the input for ML. Through the screening of the significance of the features by ML, the most important geometric and electronic parameters were obtained. The two parameters were then acted as two axes for the plotting of the catalytic hot spot map, which guided the design of the ORR catalyst through the coupling of the geometric and electronic effects. Based on the hot spot map, the ideal diatomic ORR catalyst was screened and experimentally validated to verify the effectiveness of the design principle.

Machine learning assisted high-throughput screening

In the M_1-N-M_2/NC model, M_1 (central metal) and M_2 (side metal) were selected from 11 transition metals, which were widely used for constructing ORR active sites (Fig. 2a)[23–33]. This yielded 121 structural combinations via permutations (Supplementary Data 1). To establish a robust dataset for ML training, 36 structures (approximately 30%) were randomly chosen for DFT calculations. Initially, we assessed the stability of these structures using the binding and formation energies. As shown in Fig. 2b, most M_1-N-M_2/NCs exhibited both negative formation energy and binding energy, demonstrating the stability of the M_1-N-M_2/NCs. Moreover, the M_1-N-M_2/NCs displayed more negative binding energy than the single-atom system (MNC), demonstrating the strong binding of M_1 and M_2 by the cage of bridge N and the surrounding N atoms. In addition, the dissolution potentials of the above structures were positive except for the case of Pd-N-Os/NC, suggesting the electrochemical stability (Supplementary Tables 1 and 2). We then calculated the Gibbs free energy variation of the ORR reaction pathways, which included four electronic transfer steps: $* + O_2 \rightarrow *OOH \rightarrow *O \rightarrow * OH \rightarrow * + H_2O$ (Supplementary Data 2 and Supplementary Tables 3, 4). Based on the data, the OOH*, OH* formation, and OH* desorption were possible potential determination steps (Fig. 2c). To quickly obtain the catalytic activity, we chose the overpotentials of the whole ORR steps as the targeted variables for ML.

To train reliable ML models that cover both geometric and electronic effects, we analyzed the potential features to gain a proper feature set. Firstly, the 22 common atomic properties were adapted as the initial feature set (Supplementary Table 5)[34,35]. According to the Pearson correlation coefficient matrix analysis, several features were deleted to avoid dimensional disasters (Supplementary Fig. 1), forming a subset containing 16 features. As shown in Fig. 2d, most pairwise

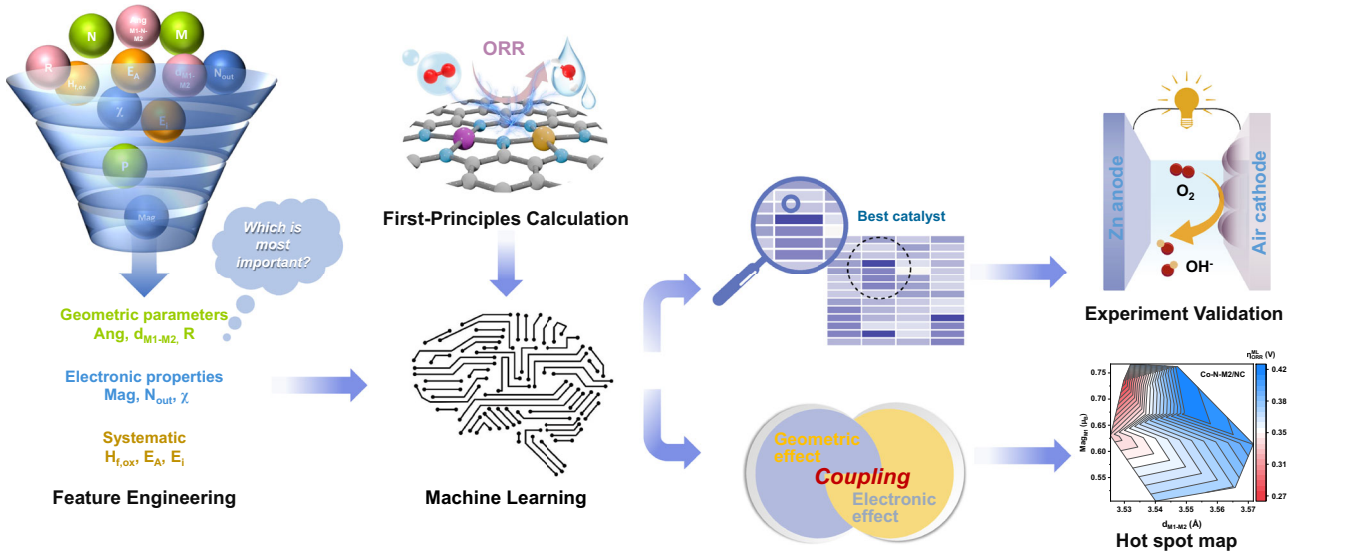

Fig. 1 | Schematic of the workflow based on the DFT-ML-experiment method to achieve a principle coupling of geometric and electronic parameters for the design of M_1-N-M_2/NCs. Some elements in this scheme were created using BioGDP.com (https://BioGDP.com).

https://doi.org/10.1038/s41467-025-60170-0

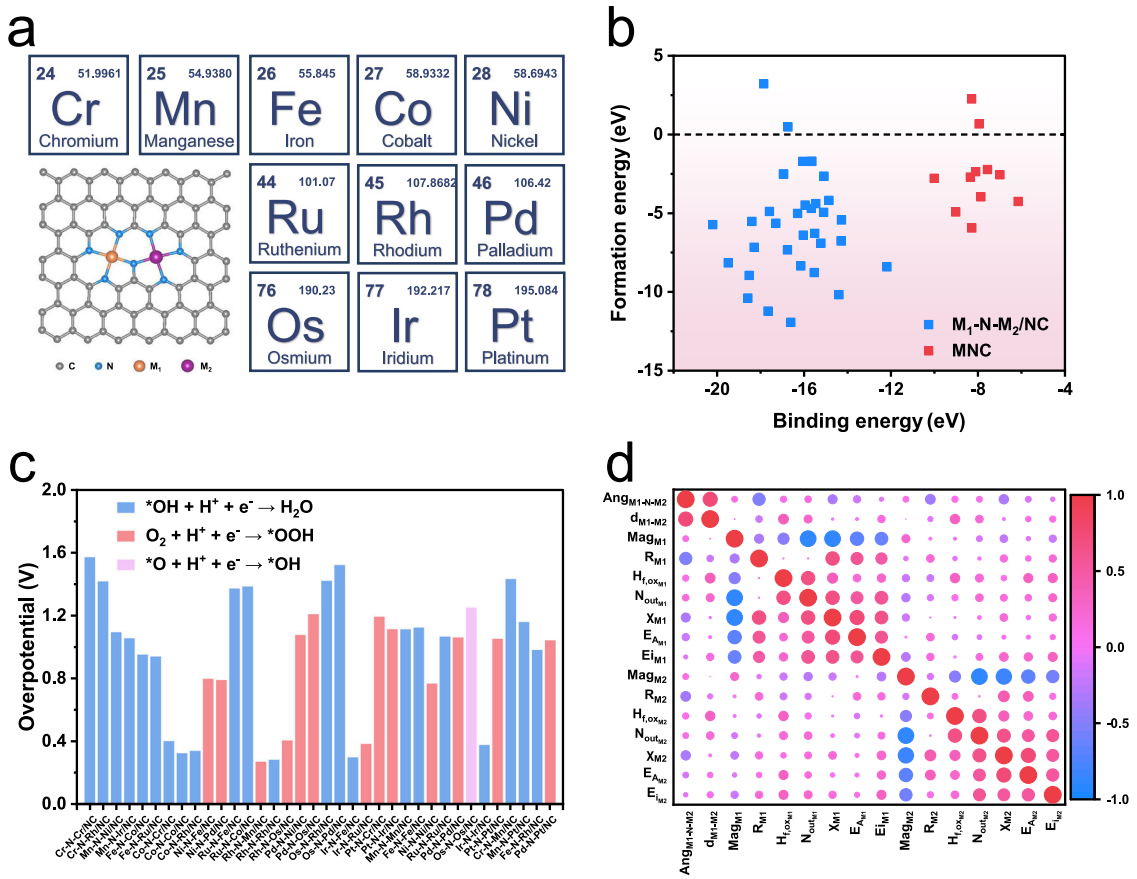

Fig. 2 | The generation and pretreatment of the data. a Schematic structure of M_1-N-M_2/NCs and element type of metal atom. **b** Binding energies and formation energies of MNC and part of the randomly combined M_1-N-M_2/NCs. **c** The overpotentials of part of the randomly combined M_1-N-M_2/NCs. **d** Pearson correlation map between each of the 16 features. Source data are provided as a Source Data file.

features of M_1-N-M_2/NCs were allowed to coexist due to the low correlation. The preserved features were categorically divided into three groups: geometric parameters ($Ang_{M1\text{-}N\text{-}M2}$, $d_{M1\text{-}M2}$, R_{M1}, R_{M2}), electronic parameters (Mag_{M1}, Mag_{M2}, χ_{M1}, χ_{M2}, N_{outM1}, N_{outM2},), and other reactive parameters ($H_{f,oxM1}$, $H_{f,oxM2}$, E_{AM1}, E_{AM2}, E_{iM1}, E_{iM2}), all of which were evenly distributed. The low linear correlation of most of the features indicated the independent and repetitive properties of the final selected features in the set, which benefited the following ML study.

In the ML model, the final selected features were used as input values, and the calculated ORR overpotentials were merged as target values. Following a systematic assessment for the impacts of training-test split ratios on predictive accuracy (Supplementary Fig. 2), we adopted an 8:2 random split of the entire dataset to ensure a balance between training sufficiency and validation reliability. After that, five different ML algorithms, including gradient boosting regression (GBR), random forest regression (RFR), support vector regression (SVR), gaussian processes regression (GPR), and K nearest neighbors regression (KNR), were used to train the corresponding models (see Supplementary Table 6 for details of these models). Subsequently, grid search and cross-validation were utilized to adjust the hyperparameters of the models, together with the root mean square error (RMSE) and coefficient of determination (R^2) evaluating the stability and accuracy of the models (Fig. 3a and Supplementary Table 7). Among the five models, the trained GBR algorithm exhibited the highest accuracy and stability in both the training set and test set. Moreover, the predicted overpotential and the DFT calculation results displayed an obvious linear relationship over the whole dataset (Fig. 3b), proving that the effective training of the GBR model achieves highly precise prediction (see Supplementary Table 8 and Supplementary Fig. 3 for detailed data and the comparison of other algorithms). Therefore, we chose the GBR algorithm to further predict the residual M_1-N-M_2/NCs outside the dataset (Fig. 3c). Ranking the overpotential from low to high values, we selected the predicted top 10 M_1-N-M_2/NCs and verified the results by DFT calculation (Fig. 3d, Supplementary Table 9 and Supplementary Data 3). The average error of the ORR overpotentials is only 0.03 V, confirming that the quick ML prediction was able to substitute the long-term DFT calculations. Specially, Co-N-Mn/NC exhibited the lowest overpotential of 0.27 V by ML prediction, corresponding to the overpotential of 0.25 V by DFT calculation (Supplementary Fig. 4). Further DFT calculations showed that Co-N-Mn/NC preferred the four-electron transfer mechanism to the two-electron transfer path for H_2O_2 generation, confirming the selectivity for ORR (Supplementary Fig. 5). According to ab initio molecular dynamics simulation, the energy of Co-N-Mn/NC fluctuated slightly, and the structures remained almost unchanged at 500 K after 12 ps, demonstrating good stability (Supplementary Fig. 6).

Interpretation of geometric and electronic descriptors

Apart from the selection of the optimal catalyst, the deep analysis of the design principle that considers both geometric and electronic effects was further conducted. Figure 4a shows the significance of the features evaluated through the SHapley Additive exPlanation (SHAP) summary plot[36]. The features were sorted vertically in descending order based on the cumulative sum of SHAP values, while the horizontal axis showcased the distribution of SHAP values for each individual feature. Among all the features, the top 3 important features were related to the intrinsic properties of M_1, indicating the species of

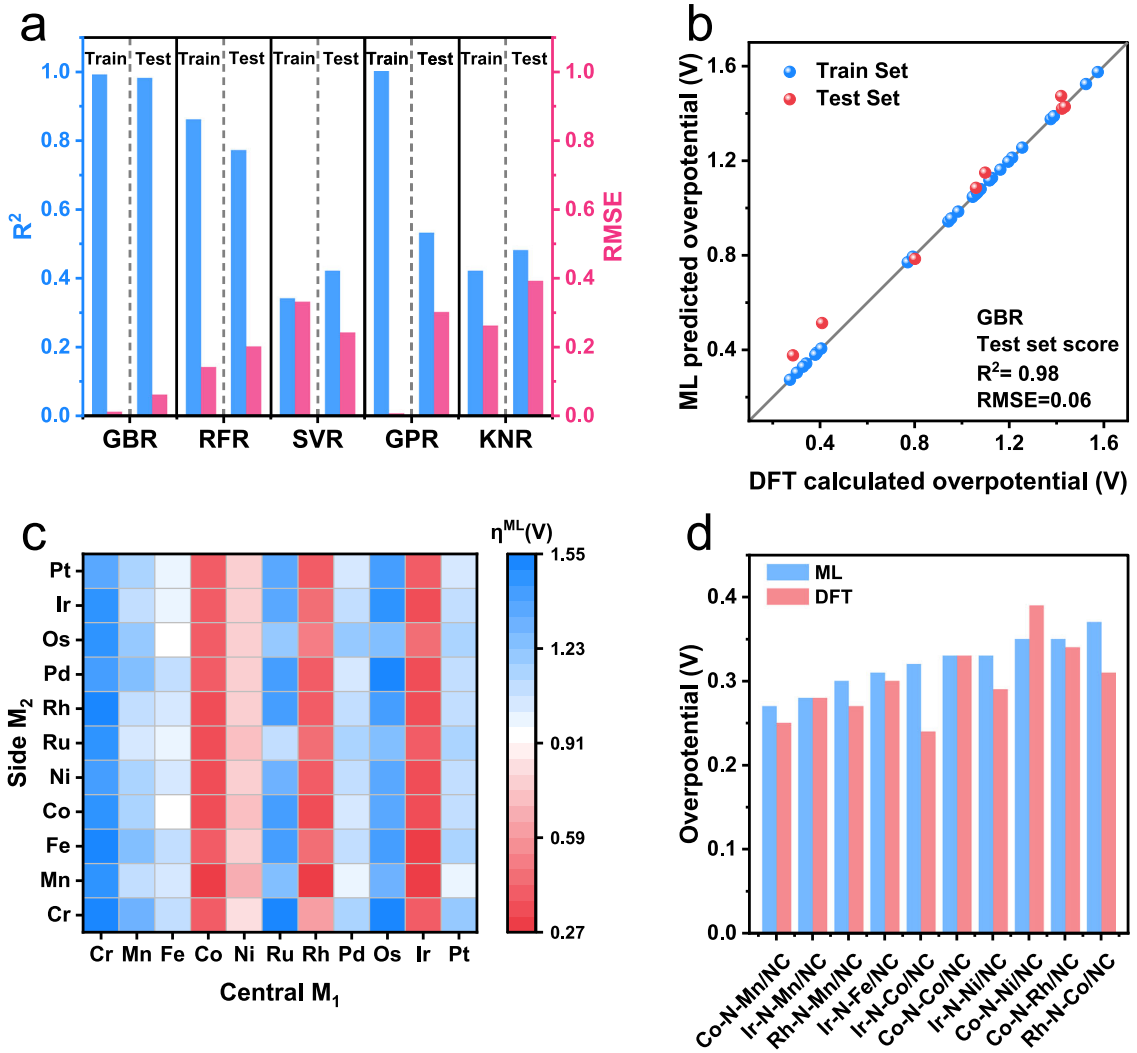

Fig. 3 | Machine learning training and prediction. a Comparison of the RMSE and the R^2 score for each model on the train set and the test set. **b** Comparison of DFT calculated overpotential values with those predicted by the best-performing GBR model. **c** ML predicted overpotential heatmap of all M_1-N-M_2/NCs in this system. **d** DFT calculations verified that ML predicted the best performing 10 M_1-N-M_2/NCs with overpotentials. Source data are provided as a Source Data file.

active center atom was the prerequisite factor for highly active ORR catalysts. The catalytic performance was boosted when the active center atom was Co, Rh, or Ir with d^7 structure, which was interestingly consistent with the e_g theory. After validating the active center, the distance of bimetallic ($d_{M1\text{-}M2}$) and the magnetic moment of M_1 (Mag_{M1}) became the top 2 determined factors. Notably, these two factors coincidentally corresponded to the geometric descriptor and electronic descriptor, respectively. This phenomenon indicated that both geometric and electronic effects can manipulate the catalytic performance, which verified the principle of catalytic action. To summarize a design principle that contained the geometric and electronic effects, we plotted the hot spot maps using $d_{M1\text{-}M2}$ and Mag_{M1} as axes and the theoretical overpotential as the mapping signal (Fig. 4b). Regardless of the species of active centers, the catalytically active signals were located within a narrow region. For the center of Co and Ir, this region required small $d_{M1\text{-}M2}$ and high Mag_{M1} values, whereas small $d_{M1\text{-}M2}$ and low Mag_{M1} values were required for the center of Rh (Supplementary Table 10). Therefore, the hot spot map served as a design principle that directed the simultaneous limitation of geometric descriptor ($d_{M1\text{-}M2}$) and electronic descriptor (Mag_{M1}). Based on the geometric-electronic coupled design principle, researchers can focus on the synergistic analysis of two key parameters rather than full-path calculations. In addition, due to narrow region for the catalytically active signals, the two key parameters are enough to quickly high-throughput screening the potential candidates for efficient catalysts, which can avoid the validation of all parameters for ML-based prediction and significantly reduce the calculation cost. Moreover, for experimental research, this hot spot map provides a clear direction for the optimization of catalyst performance by regulating the two key parameters in the narrow region of the hot spot map.

Synthesis and characterization of the predicted optimal catalyst

To further verify the reliability of the design principle, we experimentally synthesized the predicted optimal catalysts (Co-N-Mn/NC) and tested the ORR performance. Supplementary Fig. 7 schematically depicted the synthetic route to the Co-N-Mn/NC catalyst via a simple double-solvent method, in which Mn phthalocyanine (MnPc) solution was mixed with a Co-containing zeolitic imidazolate framework (Co-ZIF-8), followed by pyrolysis at 950 °C. To get more insight into the Co-Mn dual sites, Co single-atom catalyst (CoNC), Mn single-atom catalyst (MnNC), and nitrogen-doped carbon (NC) were prepared for comparison. The preparation details for these catalysts were provided in the "Methods" section. The scanning electron microscopy (SEM) and transmission electron microscopy (TEM) images of Co-N-Mn/NC displayed a dodecahedron morphology with particle size of ~100 nm (Supplementary Fig. 8 and Fig. 5a). X-ray diffraction (XRD) pattern and

https://doi.org/10.1038/s41467-025-60170-0

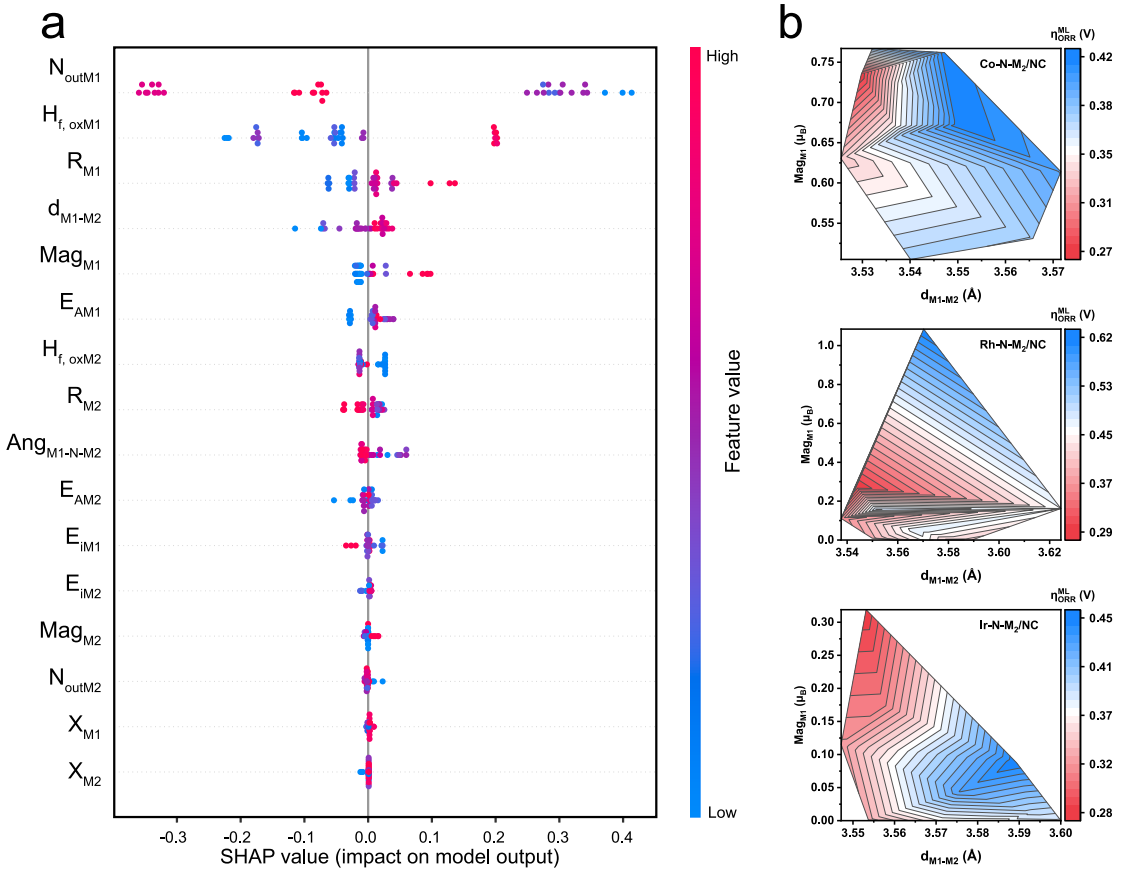

Fig. 4 | Analysis of key factors affecting catalytic performance. a SHAP summary plot of the GBR model for ORR overpotentials. **b** Hot spot plot of ML predicted overpotential as a function of $d_{M1\text{-}M2}$ and Mag_{M1} features by M_1-N-M_2/NCs (M_1 = Co, Rh, Ir). Source data are provided as a Source Data file.

high-resolution TEM (HRTEM) image for Co-N-Mn/NC revealed the absence of metal-related nanoparticles, preliminarily confirming the preparation of atomically dispersed catalysts, control catalysts (CoNC, MnNC, and NC) also showed similar morphologies and XRD patterns (Supplementary Figs. 9–11), suggesting a similar amorphous carbon structure. Meanwhile, the HRTEM image showed the presence of graphitized carbon layers, which were conducive to electronic conduction. Moreover, Raman spectra displayed a close intensity ratio of *D*-band to *G*-band (I_D/I_G) for all catalysts, indicating that as-synthesized catalysts exhibited similar defect degrees (Supplementary Fig. 12). In addition, N_2 adsorption/desorption isotherm curves showed that the BET specific surface areas of Co-N-Mn/NC, CoNC, and MnNC were 529, 731, and 737 $m^2 g^{-1}$, respectively (Supplementary Fig. 13). All these catalysts possessed abundant micropores, beneficial for the exposure of catalytic active sites.

We further studied the structure of Co-N-Mn/NC at the atomic resolution. In the aberration-corrected HAADF-STEM (AC HAADF-STEM) image, abundant bright dots were distributed in pairs within the carbon matrix, illustrating the possible coexistence of Co-Mn dual sites within Co-N-Mn/NC (Fig. 5b). According to the estimation of the distance between the pair dot, the adjacent Co and Mn atoms possessed the distance of 3.56 Å, which was consistent with the structure of N-bridged diatoms (Fig. 5c). Compared with the paired dual dots for Co-N-Mn/NC, plenty of isolated bright dots were observed in AC HAADF-STEM images of CoNC and MnNC, corresponding to the atomically dispersed Co sites and Mn sites, respectively (Supplementary Fig. 14). Figure 5d shows the high-angle annular dark-field scanning TEM (HAADF-STEM) and corresponding energy-dispersive X-ray spectroscopy (EDS) mapping images of Co-N-Mn/NC, displaying the uniform elemental distribution of Co, Mn, and N throughout the whole carbon matrix.

To determine the electronic environments and chemical bonding nature for Co-N-Mn/NC and controls, we performed a series of characterizations. In N 1*s* X-ray photoelectron spectroscopy (XPS) spectra, metal-nitrogen bonds were clearly recorded (Supplementary Fig. 15a). Notably, pyridinic-N was the primary species in all catalysts, which was consistent with our theoretical model of Co-N-Mn/NC. No cobalt nitride, manganese nitride, or Co/Mn-related metal nanoparticles peaks were detected for Co-N-Mn/NC, CoNC, and MnNC in their Co 2*p* and Mn 2*p* XPS spectra (Supplementary Fig. 15b, c), implying the possible existence of N bonded to Co or Mn in our catalysts, respectively. In Co K-edge X-ray absorption near-edge structure (XANES) spectra, the Co K-pre-edges of both CoNC and Co-N-Mn/NC lay between those of Co foil and CoPc, suggesting that the Co oxidation states resided between 0 and +2 (Supplementary Fig. 16a). In Fig. 5e, the Co K-edge extended X-ray absorption fine structure (EXAFS) spectra for both Co-N-Mn/NC and CoNC exhibited a singular peak located at roughly 1.53 Å, ascribing to the first shell CoN scattering path[28]. Meanwhile, no peak referring to the CoCo path at 2.18 Å was observed[37], verifying the atomic dispersion of Co atoms within both Co-N-Mn/NC and CoNC. According to the XANES and EXAFS of Mn, the similar result of atomic dispersion was concluded in the case of Mn elements in Co-N-Mn/NC and MnNC (Fig. 5f and Supplementary Fig. 16b)[38]. Additionally, compared to CoNC and MnNC, the CoN and MnN peaks in EXAFS of Co-N-Mn/NC were asymmetric and slightly shifted, indicating that the coupling of adjacent Co and Mn atoms affected the coordination environment of the metal center. As illustrated in the EXAFS fitting of Co-N-Mn/NC, both Co and Mn atoms were coordinated with the four N atoms in the first shell, corresponding to CoNC and MnNC (Fig. 5g, h and Supplementary Tables 11, 12).

https://doi.org/10.1038/s41467-025-60170-0

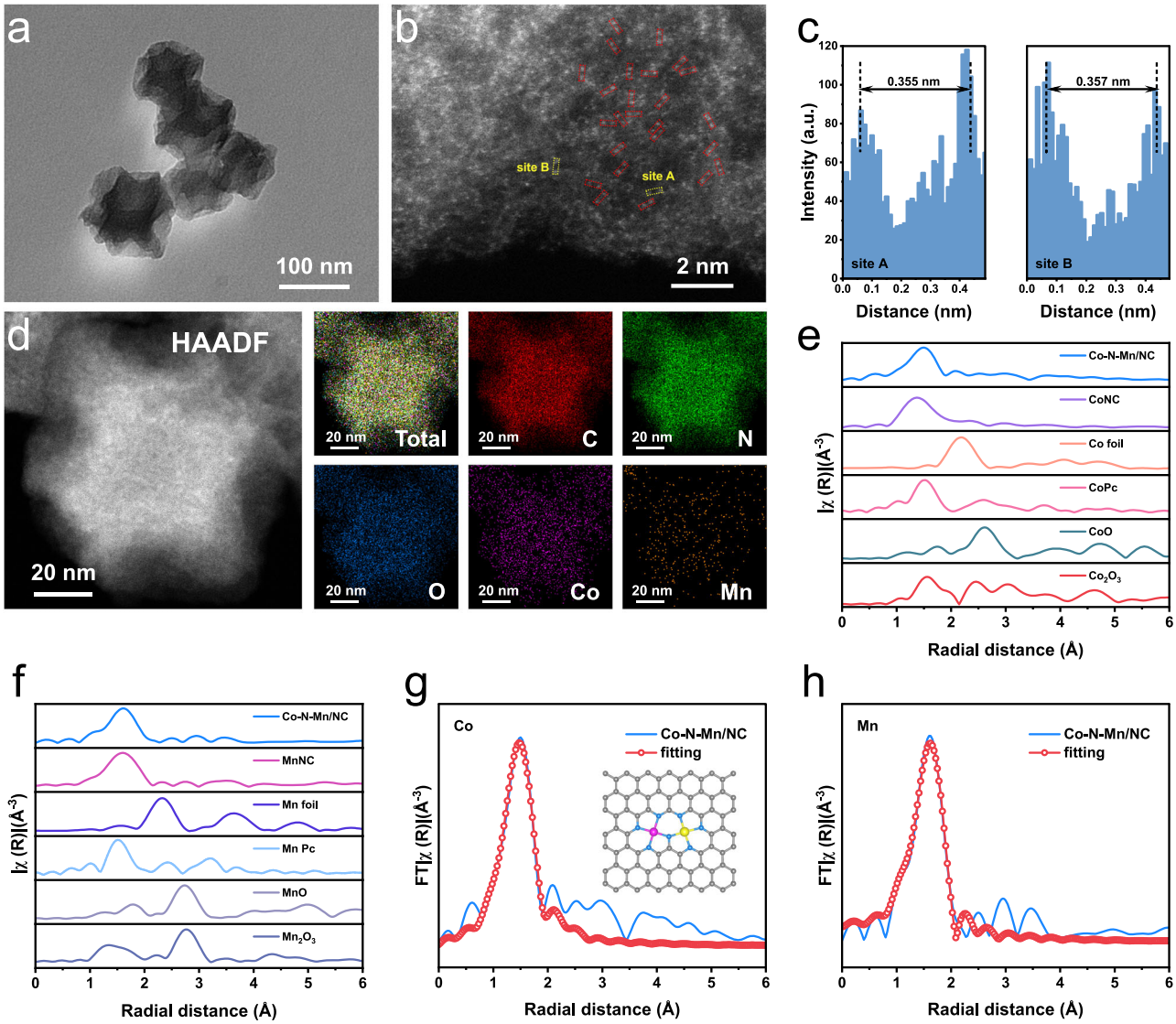

Fig. 5 | Characterization of Co-N-Mn/NC catalyst. a TEM and **b** AC HAADF-STEM images of Co-N-Mn/NC catalyst. **c** The intensity profiles obtained on site A and site B. **d** Corresponding EDS mapping images of Co-N-Mn/NC catalyst. **e** The EXAFS spectra of Co K-edge in R space. **f** The EXAFS spectra of Mn K-edge in R space. **g** The R-space EXAFS fitting curves of the Co-N-Mn/NC at Co K-edge. Inset: Schematic diagram of the Co-N-Mn/NC structure. **h** The R-space EXAFS fitting curves of the Co-N-Mn/NC at Mn K-edge. Source data are provided as a Source Data file.

Electrochemical performance testing of the predicted optimal catalyst

The ORR electrocatalytic performance of Co-N-Mn/NC and controls was evaluated using a three-electrode system with a rotating disk electrode (RDE) in 0.1 M KOH electrolyte (Supplementary Fig. 17). The linear sweep voltammetry (LSV) curves indicated that the Co-N-Mn/NC exhibited the highest ORR activity over reference catalysts, featuring a half-wave potential ($E_{1/2}$) of 0.900 V superior to those of CoNC (0.871 V), MnNC (0.839 V), NC (0.768 V), and Pt/C (0.883 V) (Fig. 6a, Supplementary Figs. 18, 19 and Supplementary Table 13). Meanwhile, the Co-N-Mn/NC exhibited higher kinetic current density (48.64 mA cm^{-2}) at 0.85 V and lower Tafel slope (54.0 mV dec^{-1}) than those of the other reference catalysts and Pt/C (Fig. 6b, c). Supplementary Fig. 20 showed that Co-N-Mn/NC possessed higher double layer capacitance (C_{dl}) compared to CoNC, MnNC, and NC, suggesting larger electrochemically active surface areas and thus more exposed ORR active sites for Co-N-Mn/NC. In addition, the results of rotating ring disk electrode (RRDE) measurements revealed that Co-N-Mn/NC delivered high catalytic selectivity with a favorable 4-electron transfer pathway toward ORR (Fig. 6d), in agreement with the results obtained from Koutecky-Levich (K-L) plots (Supplementary Fig. 21). As shown by the accelerated durability test and chronoamperometric test, the Co-N-Mn/NC catalyst exhibited a negligible decay in terms of $E_{1/2}$ after 10,000 continuous CV cycles and maintained a high current density retention after 13 h of continuous operation at 0.7 V, manifesting its remarkable durability (Fig. 6e, f). In addition, unlike the Pt/C catalyst, the Co-N-Mn/NC catalyst exhibited tolerance to methanol (Supplementary Fig. 22). These results suggested the highly active and stable of Co-N-Mn/NC towards ORR catalysis.

To further confirm the remarkable ORR activity and stability of Co-N-Mn/NC, an aqueous ZAB with Co-N-Mn/NC as cathodic catalyst was assembled. The as-constructed ZAB with the Co-N-Mn/NC cathode achieved a high open-circuit voltage (OCV) of 1.51 V (Fig. 7a), a large peak power density of 271 mW cm^{-2}, exceeding the Pt/C-based ZAB (OCV: 1.45 V, peak power density: 186 mW cm^{-2}) (Fig. 7b). Moreover, Co-N-Mn/NC-based ZAB also showed a better rate performance at different current densities from 1 to 50 mA cm^{-2} and a higher specific capacity (806 mAh g^{-1}_{Zn}) than those of the Pt/C-based ZAB (653 mAh g^{-1}_{Zn}) (Fig. 7c, d). Moreover, the Co-N-Mn/NC-based ZAB showed high stability over 200 h of discharge-charge cycling test at

https://doi.org/10.1038/s41467-025-60170-0

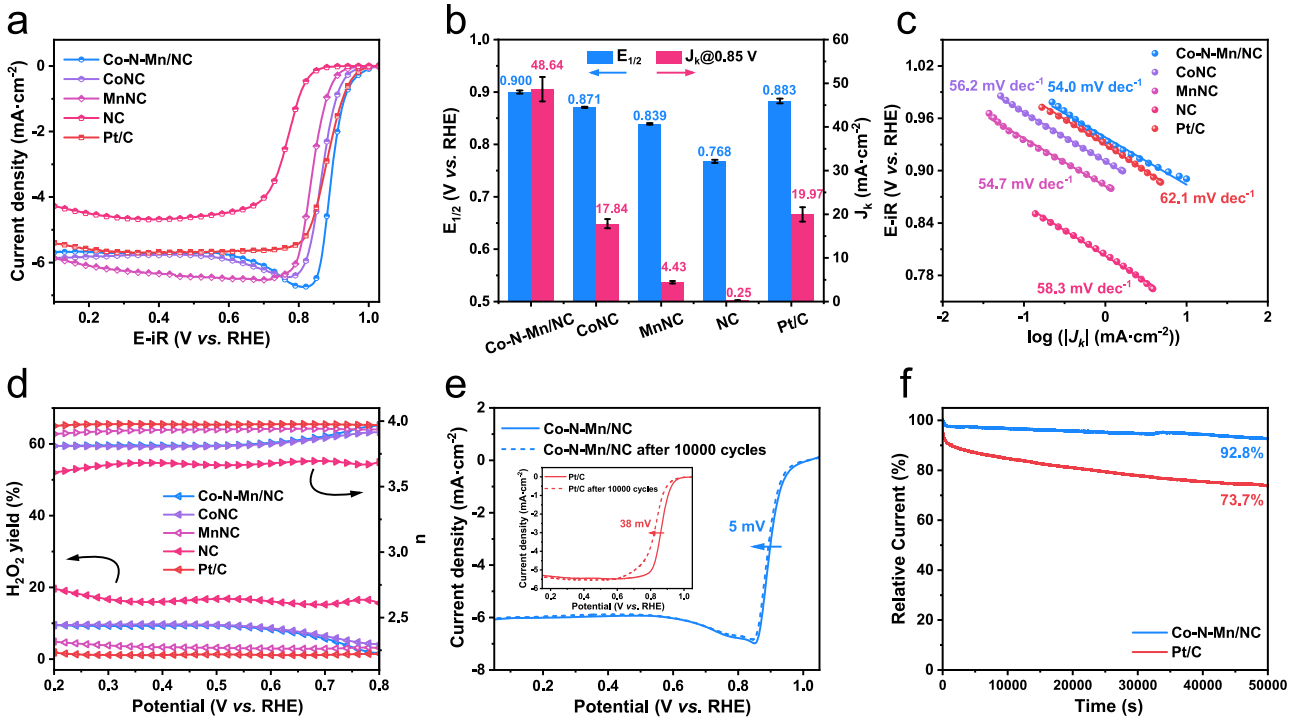

Fig. 6 | Electrochemical activity of Co-N-Mn/NC catalyst. a iR-corrected RDE polarization curves of Co-N-Mn/NC, CoNC, MnNC, NC, and Pt/C catalysts (scan rate: 5 mV s^{-1}, rotation rate: 1600 rpm). **b** Comparison of $E_{1/2}$ and J_k at 0.85 V for the different catalysts. **c** Corresponding Tafel plots derived from the RDE polarization curves for the different catalysts. The error bars are the standard deviations of three individual calculations. **d** Electron transfer number (n) and H_2O_2 yield of Co-N-Mn/NC and the reference catalysts. **e** Accelerated durability test of Co-N-Mn/NC catalyst before and after 10,000 continuous CV cycles ranging from 0.7 to 1.0 V (vs. RHE). Inset: accelerated durability test of Pt/C catalyst. **f** Chronoamperometric test of Co-N-Mn/NC and Pt/C catalysts at 0.7 V. Source data are provided as a Source Data file.

5 mA cm^{-2}, whereas the commercial Pt/C + IrO_2-based battery suffered from severe degradation after about 70 h (Fig. 7e). Through using the catalytically active and stable Co-N-Mn/NC-based ZAB, a toy light was powered by two in series connected ZABs, showing promising application prospects of Co-N-Mn/NC in energy storage devices (Supplementary Fig. 23).

The comparison of design method and catalyst performance

To display the advancement of our design method and catalyst performance, we provided a comparison relative to the reported literature from both theoretical and experimental aspects. As shown in Fig. 8a, the theoretical overpotential of the predicted Co-N-Mn/NC catalyst was compared with that of the reported Pt-free catalyst. Our DFT-calculated overpotential (0.25 V) was one of the lowest values among the listed catalysts (the detailed data for comparison can be seen in Supplementary Table 14), indicating the effectiveness of geometric-electronic coupled design for ORR catalyst. To gain the geometric and electronic descriptors, the time cost by DFT calculations was 5.67 h. Using the ML-derived hot-spot map, we only took 20 s to obtain the overpotentials of the 85 diatomic models in the predicting dataset and precisely found the optimal Co-N-Mn model. To get similar results, traditional DFT-based high throughput screening required ~1071 h, which was 188-fold longer than the current ML-DFT coupled method (Fig. 8b). This result indicated the advantage of our geometric-electronic coupled design combining ML and DFT calculations.

The experimental performance of the Co-N-Mn/NC catalyst toward ORR and ZAB was further evaluated with those of the previously reported Pt-free materials. For the ORR, the $E_{1/2}$ and the J_k at 0.85 V were two key parameters for the evaluation of the performance. Compared with other reported Pt-free catalysts, the Co-N-Mn/NC was located at the upper-right region in Fig. 8c (the detailed data for comparison can be seen in Supplementary Table 15), indicating the remarkable performance with high $E_{1/2}$ and high J_k values. Furthermore, compared with recently reported Co-Mn dual-site catalysts (Supplementary Fig. 24 and Table 16), Co-N-Mn/NC exhibited the highest half-wave potential in alkaline media, further demonstrating its superior performance as an efficient ORR catalyst. The performance of ZAB device was another aspect to assess the Co-N-Mn/NC catalyst for potential practical use, which mainly considered the peak power density and specific activity. Among the listed materials, the Co-N-Mn/NC exhibited the highest peak power density with a relatively high specific activity, demonstrating the superiority of Co-N-Mn/NC for the battery device (Fig. 8d and Supplementary Table 17). Taken together, the highly efficient Co-N-Mn/NC catalyst demonstrated the success of the geometric-electronic coupled design for ORR catalyst.

Discussion

In summary, we developed a geometric-electronic coupled design principle through a catalytic hot spot map for diatomic ORR catalysts by machine learning. In this hot spot map, the geometric parameter $d_{M1\text{-}M2}$ and electronic parameter Mag_{M1} were recognized as the two descriptors that manipulated the catalytic properties of active center atoms. For a certain active center atom, the highly active region in the hot spot map was narrow, which can direct the design of diatomic ORR catalysts. Based on this design, we predicted a highly active ORR catalyst of Co-N-Mn/NC and verified this result by experiment. The Co-N-Mn/NC catalyst exhibited $E_{1/2}$ of 0.90 V and J_k of 48.64 mA cm^{-2} at 0.85 V, with a peak power density of 271 mW cm^{-2} and a specific capacity of 806 mAh g^{-1}_{Zn} toward ZAB tests. Our work not only showed the successful prediction of ORR catalysts, but also provided a protocol for finding coupled design principles for catalysts with both geometric and electronic factors.

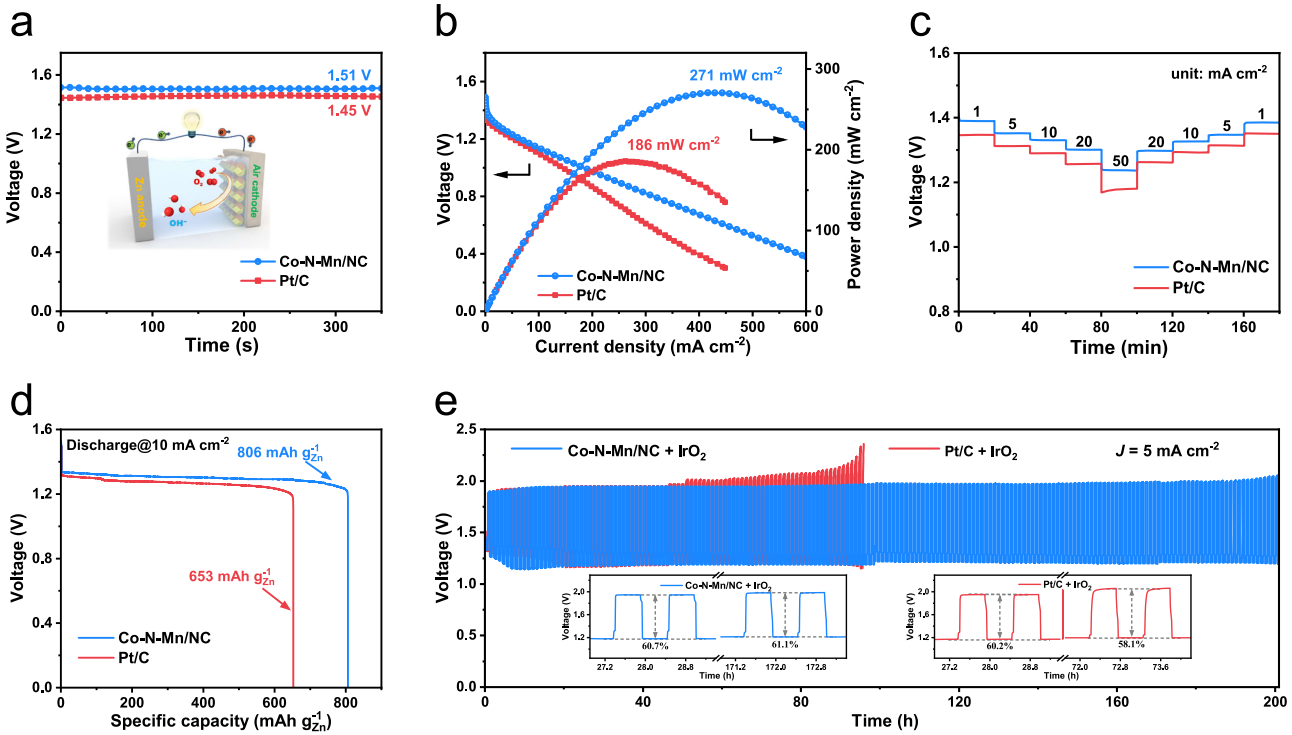

Fig. 7 | Zinc air battery based on Co-N-Mn/NC catalyst. a An Open-circuit voltage. Inset: Schematic illustration of a ZAB. **b** Polarization curve and the recorded power density for the Co-N-Mn/NC or commercial Pt/C catalyst-based ZAB, respectively. **c** Rate performance of the ZABs with Co-N-Mn/NC or commercial Pt/C as air-cathode at different current densities. **d** Galvanostatic discharge curves of Co-N-Mn/NC or commercial Pt/C-based ZAB at $j = 10$ mA cm^{-2}. **e** Long-term discharge-charge curves at $j = 5$ mA cm^{-2} for ZABs with Co-N-Mn/NC+ IrO_2 and commercial Pt/C + IrO_2. Inset: the corresponding voltage efficiency curves during the cycling test. Source data are provided as a Source Data file.

Methods

DFT computational details

Spin-polarized DFT calculations were performed using the Vienna ab initio simulation package (VASP) 5.4.4 code[39]. The exchange-correlation energy was modeled by the Perdew-Burke-Ernzerhof (PBE) functional within the generalized gradient approximation (GGA)[40], and the projector augmented wave (PAW) pseudo-potentials were used to describe the ionic cores[41]. A vacuum space of 15 Å was adopted in the z-direction of the $6 \times 6 \times 1$ graphene supercell to minimize interactions among neighboring catalyst images. The cutoff energy was set as 500 eV and the Brillouin zone was sampled using $3 \times 3 \times 1$ k-points. The convergence criteria of structure optimization were chosen as the maximum force on each atom less than 0.02 eV/Å with an energy change less than 1×10^{-5} eV. The van der Waals interaction was treated by using the empirical correction in Grimme's scheme (DFT-D2)[42]. More computational details can be found in the Supplementary Information.

Machine learning computational details

All ML algorithms were conducted by the open-source code Scikit-learn in the Python3 environment[43]. Given the limited sample size and high feature dimensionality of the dataset in this work, we employed five distinct regression algorithms under a supervised learning framework to construct predictive models. These algorithms encompassed various paradigms, including ensemble learning, kernel methods, probabilistic modeling, and lazy learning, providing multi-faceted insights into the relationship between data features and the target variable. Detailed theoretical formulations, applicability conditions, and algorithmic advantages of each algorithm were provided in the Supplementary Information. Two indicators used to describe prediction errors, the RMSE and R^2 score, were applied herein to evaluate the accuracy of the ML models. Their expressions were as follows:

$$R^2 = 1 - \frac{\frac{1}{n}\sum_{i=1}^{n}(y_i - \hat{y}_i)^2}{\frac{1}{n}\sum_{i=1}^{n}(y_i - \mu_i)^2} \quad (1)$$

$$RMSE = \sqrt{\frac{1}{n}\sum_{i=1}^{n}(y - \hat{y}_i)^2} \quad (2)$$

where $\hat{y}_i$, y_i, and μ_i denote the ground truth, the prediction of the model, and the mean value, respectively. The R^2 score ranged from 0 to 1, and the prediction accuracy of the model was desired when the R^2 score approached the value of 1. The RMSE represented the loss between the prediction and the ground truth. The lower RMSE loss meant a better model performance.

Materials and chemicals

Zinc (II) nitrate hexahydrate ($Zn(NO_3)_2{\cdot}6H_2O$, 99%, Aladdin), cobalt (II) nitrate hexahydrate ($Co(NO_3)_2{\cdot}6H_2O$, 99%, Macklin), manganese phthalocyanine (MnPc, 98%, Rhawn), 2-methylimidazole (2-mIm, 98%, Aladdin), n-hexane (99%, Macklin), and methanol (99.9%, Macklin) were used as received without further purification. Deionized water (18.25 MΩ cm) used in the experiments was obtained from an ultrapure purification system (EPED).

Catalysts preparation

We synthesized Co-N-Mn/NC and a series of comparative catalysts through a simple dual solvent method. Initially, 2-mIm (2.42 g) was dissolved in 50 mL of methanol with stirring in a flask, obtaining solution A. Concurrently, $Zn(NO_3)_2{\cdot}6H_2O$ (1.38 g) and $Co(NO_3)_2{\cdot}6H_2O$ (0.08 g) were dissolved in 50 mL of methanol under ultrasound for 5 min to form a clear solution B. Then, solution A was added to solution

https://doi.org/10.1038/s41467-025-60170-0

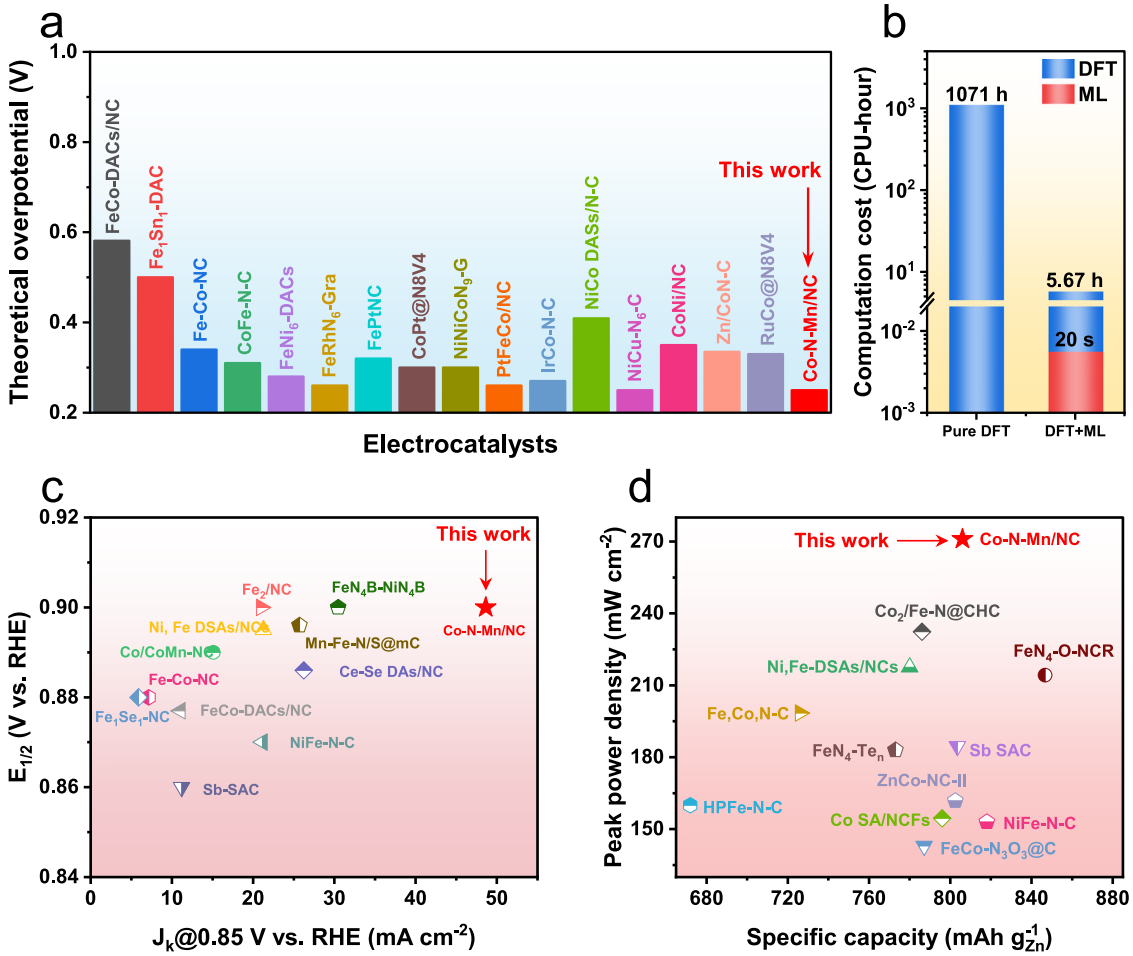

Fig. 8 | Comparison of design method and catalyst performance. a Comparison of theoretical overpotential values for Co-N-Mn/NC and catalysts in literature. **b** Comparison of the average computation costs for predicting the ORR catalytic activity of residual M_1-N-M_2/NC using pure DFT calculation and ML prediction. **c** Comparison of the J_k and $E_{1/2}$ values between Co-N-Mn/NC and the catalysts reported recently. **d** Comparison of peak power density and specific capacity of Co-N-Mn/NC and recently reported highly active catalysts. The detailed data and references for comparison can be seen in the Supplementary Information tables. Source data are provided as a Source Data file.

B under stirring at 800 rpm for 24 h. The resulting product was separated by centrifugation, washed three times with methanol, and then vacuum-dried at 80 °C overnight to obtain Co-ZIF-8. The ZIF-8 was also synthesized using the same method as Co-ZIF-8, but without the addition of cobalt nitrate hexahydrate. Next, the as-prepared Co-ZIF-8 (0.05 g) was dispersed in 13 mL of n-hexane, followed by sonicated for 30 min, obtaining a well-distributed suspension. Subsequently, 0.015 mL of MnPc solution (50 mg mL^{-1}, MnPc in ethanol) was added dropwise into the above suspension under continuous sonication for 15 min, followed by vigorous stirring for 2 h. The resulting suspension was centrifuged, washed with ethanol, and finally dried at 80 °C overnight to yield MnPc@Co-ZIF-8. The MnPc@ZIF-8 was prepared using the same method as MnPc@Co-ZIF-8 by replacing Co-ZIF-8 with ZIF-8. The aforementioned precursors (MnPc@Co-ZIF-8, Co-ZIF-8, MnPc@ZIF-8, and ZIF-8) were fully ground and pyrolyzed in a tube furnace under argon gas at 950 °C for 2 h (heating rate of 5 °C min^{-1}), obtaining Co-N-Mn/NC, CoNC, MnNC, and NC, respectively.

Physical characterization

The structure of the samples was characterized by a Bruker D2 Phaser XRD equipped with a Cu-K radiation source. Morphology characterization was performed on a Zeiss Gemini 300 SEM and Hitachi HT7700 TEM. High-resolution TEM images were determined by using a Talos F200S-G2 HRTEM operated at 200 kV. HAADF-STEM images were obtained using a JEOL ARM-200F HAADF-STEM equipped with EDS, operated at 300 kV. Co K-edge and Mn K-edge XANES spectra were collected at the commercial Laboratory-Based XAFS spectrometer (Rapid XAFS 1 M, Anhui Absorption Spectroscopy Analysis Instrument Co., Ltd). Raman data were collected on a Horiba LabRAM HR Evolution Raman spectrometer (laser wavelength is 532 nm). XPS experiments were conducted on a Thermo Fisher Nexsa spectrometer. N_2 adsorption-desorption isotherms of all samples were measured using a Micromeritics ASAP 2460 N_2 adsorption instrument.

ORR performance measurements

The ORR performance was measured in a three-electrode configuration using a CHI 760 C electrochemical workstation at room temperature (298.15 K). A catalyst loaded RDE with a glassy carbon (GC) disk of 5 mm in diameter or a RRDE with a Pt ring (6.25 mm ring inner diameter and 7.92 mm ring outer diameter) and a GC disk of 5.61 mm in diameter were used as working electrode. An Ag/AgCl (saturated KCl) and a graphite rod were used as reference and counter electrodes, respectively. All the potentials were calibrated with respect to the reversible hydrogen electrode (RHE) according to the following equations:

$$E_{RHE} = E_{Ag/AgCl} + 0.197 + 0.0592 \times pH \quad (3)$$

The Ag/AgCl electrode was calibrated using a three-electrode system configuration, where the reference electrode served as the reference, a platinum sheet as the working electrode, and a platinum sheet as the counter electrode. Hydrogen gas remained saturated in the 0.1 M KOH electrolyte throughout the test. CV was performed over a potential range of −1.05 V to −0.85 V at a scan rate of 1 mV s^{-1} to maintain equilibrium conditions in the reaction system. The calibrated potential of the reference electrode was determined by averaging the two electrode potentials corresponding to the zero current density points in the CV measurement.

To prepare the working electrode, a homogeneous catalyst ink was first prepared by dispersing 5 mg of the sample into 1 mL of a mixture solution containing 0.495 mL of isopropyl alcohol, 0.495 mL of deionized water, and 10 μL of Nafion solution (5 wt%) by the assistance of ultrasonication for 1 h. Thereafter, 20 μL of catalyst ink (0.1 mg of sample) was dropped onto the GC surface (0.196 cm^2 of geometric area) to obtain the working electrode with a catalyst loading of 0.50 mg cm^{-2}.

Before each electrochemical experiment, N_2 or O_2 gas was bubbled into the electrolyte for about 30 min, obtaining the N_2 or O_2-saturated solution. The 0.1 M KOH electrolyte was prepared fresh before use and stored in an airtight to prevent moisture absorption and deterioration. The CV tests were conducted in O_2-saturated 0.1 M KOH solution from 1.0 to 0 V (vs. RHE) with a scan rate of 50 mV s^{-1} for activation and stabilization tests. RDE/RRDE tests were measured in N_2 or O_2-saturated 0.1 M KOH solution at 1600 rpm from 1.0 to 0 V (vs. RHE) with a sweep rate of 5 mV s^{-1}. Electrochemical impedance spectroscopy (EIS) tests were conducted in O_2-saturated electrolyte solutions under AC voltage amplitude of 5 mV in the frequency range of 1000 kHz to 0.01 Hz.

The number of electrons transferred (n) for the ORR at various electrode potentials was determined by the Koutecky-Levich equation:

$$\frac{1}{J} = \frac{1}{J_L} + \frac{1}{J_K} = \frac{1}{B\omega^{1/2}} + \frac{1}{J_K} \tag{4}$$

$$B = 0.62nF(D_0)^{2/3}(\upsilon)^{-1/6}C_0 \tag{5}$$

where J is the measured current density, J_K and J_L are the kinetic and limiting current densities, ω is the rotating speed of the working electrode, B is the Levich constant, n is the electron transfer number, F is the Faraday constant (F = 96,485 C mol^{-1}), D_0 is the diffusion coefficient of O_2 in 0.1 M KOH (1.9×10^{-5} cm^2 s^{-1}), C_0 is the bulk concentration of O_2 in 0.1 M KOH (1.2×10^{-6} mol cm^{-3}), and v is the kinetic viscosity of the electrolyte (1×10^{-2} cm^2 s^{-1}).

The hydrogen peroxide yield (H_2O_2%) and n were calculated using the following equations:

$$n = 4 \times \frac{I_d}{I_d + I_r/N} \tag{6}$$

$$H_2O_2\% = 200 \times \frac{I_r}{I_r + NI_d} \tag{7}$$

where I_d is the disk current, I_r is the ring current, and N is the current collection efficiency of the Pt ring, which is 0.37.

Zn-air battery tests

A liquid Zn-air battery was tested in homemade electrochemical cells, where the as-prepared catalysts loaded carbon paper (catalyst loading: 1 mg cm^{-2}), Zn plate, and 6.0 M KOH were used as air cathode, anode, and electrolyte, respectively. Battery performance was measured under an ambient atmosphere in an incubator at 298.15 K using a LAND CT2001A electrochemical workstation. For the long-term discharge-charge cycling test, 6.0 M KOH with 0.2 M zinc acetate was used as the electrolyte to ensure reversible Zn electrochemical reactions at the anode. Besides, catalysts (Co-N-Mn/NC or Pt/C) mixed with IrO_2 in a mass ratio of 1:1 were used to prepare the air electrode.

Data availability

The data that supports the findings of the study are included in the main text and Supplementary Information files. Source data are provided with this paper.

Code availability

The codes used to train models for predicting the theoretical potentials of ORR are available on GitHub at https://github.com/YanYang233/ORR-ML.git[44].

References

1. Kment, S. et al. Single atom catalysts based on earth-abundant metals for energy-related applications. *Chem. Rev.* **124**, 11767–11847 (2024).
2. Bai, L., Hsu, C.-S., Alexander, D. T. L., Chen, H. M. & Hu, X. Double-atom catalysts as a molecular platform for heterogeneous oxygen evolution electrocatalysis. *Nat. Energy* **6**, 1054–1066 (2021).
3. Wang, Q., Cheng, Y., Yang, H. B., Su, C. & Liu, B. Integrative catalytic pairs for efficient multi-intermediate catalysis. *Nat. Nanotechnol.* **19**, 1442–1451 (2024).
4. Fang, C. et al. Synergy of dual-atom catalysts deviated from the scaling relationship for oxygen evolution reaction. *Nat. Commun.* **14**, 4449 (2023).
5. Zhang, W. et al. Emerging dual-atomic-site catalysts for efficient energy catalysis. *Adv. Mater.* **33**, e2102576 (2021).
6. Pu, T. et al. Dual atom catalysts for energy and environmental applications. *Angew. Chem. Int. Ed.* **62**, e202305964 (2023).
7. Wang, X. et al. Developing a class of dual atom materials for multifunctional catalytic reactions. *Nat. Commun.* **14**, 7210 (2023).
8. Li, M. et al. Spin-polarized PdCu-Fe_3O_4 in-plane heterostructures with tandem catalytic mechanism for oxygen reduction catalysis. *Adv. Mater.* **36**, e2412004 (2024).
9. Zhao, Y. et al. Steric-confinement Rh_2/MoS_2 dual-atom catalyst directionally modulating adsorption configuration of ester group to boost ethanol synthesis. *Chem* **10**, 3342–3363 (2024).
10. Ren, C. et al. A universal descriptor for complicated interfacial effects on electrochemical reduction reactions. *J. Am. Chem. Soc.* **144**, 12874–12883 (2022).
11. Chen, S. et al. Dehydrogenation of ammonia borane by platinum-nickel dimers: Regulation of heteroatom interspace boosts bifunctional synergetic catalysis. *Angew. Chem. Int. Ed.* **61**, e202211919 (2022).
12. Zhou, J. et al. Precisely tailoring the d-band center of nickel sulfide for boosting overall water splitting. *Appl. Catal. B* **359**, 124461 (2024).
13. Jiang, S. et al. Visualization of the distance-dependent synergistic interaction in heterogeneous dual-site catalysis. *J. Am. Chem. Soc.* **146**, 29084–29093 (2024).
14. Zhang, L. et al. High-density asymmetric iron dual-atom sites for efficient and stable electrochemical water oxidation. *Nat. Commun.* **15**, 9440 (2024).
15. Wang, H. et al. Disentangling the size-dependent geometric and electronic effects of palladium nanocatalysts beyond selectivity. *Sci. Adv.* **5**, eaat6413 (2019).
16. Li, Z. et al. Geometric and electronic engineering of atomically dispersed copper-cobalt diatomic sites for synergistic promotion of bifunctional oxygen electrocatalysis in zinc-air batteries. *Adv. Mater.* **35**, e2300905 (2023).
17. Zhao, S.-N., Li, J.-K., Wang, R., Cai, J. & Zang, S.-Q. Electronically and geometrically modified single-atom Fe sites by adjacent Fe nanoparticles for enhanced oxygen reduction. *Adv. Mater.* **34**, e2107291 (2022).

18. Yang, P., Li, J., Vlachos, D. G. & Caratzoulas, S. Tuning active site flexibility by defect engineering of graphene ribbon edge-hosted Fe-N_3 sites. *Angew. Chem. Int. Ed.* **63**, e202311174 (2024).
19. Li, R. et al. Polystyrene waste thermochemical hydrogenation to ethylbenzene by a N-bridged Co, Ni dual-atom catalyst. *J. Am. Chem. Soc.* **145**, 16218–16227 (2023).
20. Chen, H. et al. Theoretical screening of cooperative N-bridged dual-atom sites for efficient electrocatalytic nitrogen reduction with remolding insight. *Nano Res.* **17**, 3413–3422 (2023).
21. Liu, Y. et al. Atomically inner tandem catalysts for electrochemical reduction of carbon dioxide. *Energy Environ. Sci.* **16**, 5185–5195 (2023).
22. Pei, J. et al. N-bridged Co-N-Ni: new bimetallic sites for promoting electrochemical CO_2 reduction. *Energy Environ. Sci.* **14**, 3019–3028 (2021).
23. Zeng, R. et al. Origins of enhanced oxygen reduction activity of transition metal nitrides. *Nat. Mater.* **23**, 1695–1703 (2024).
24. Chang, J. et al. Improving Pd-N-C fuel cell electrocatalysts through fluorination-driven rearrangements of local coordination environment. *Nat. Energy* **6**, 1144–1153 (2021).
25. Tao, L. et al. Precise synthetic control of exclusive ligand effect boosts oxygen reduction catalysis. *Nat. Commun.* **14**, 6893 (2023).
26. Tang, B. et al. A janus dual-atom catalyst for electrocatalytic oxygen reduction and evolution. *Nat. Synth.* **3**, 878–890 (2024).
27. Zhao, C.-X. et al. A clicking confinement strategy to fabricate transition metal single-atom sites for bifunctional oxygen electrocatalysis. *Sci. Adv.* **8**, eabn5091 (2022).
28. Lv, M. et al. Precisely engineering asymmetric atomic CoN_4 by electron donating and extracting for oxygen reduction reaction. *Angew. Chem. Int. Ed.* **63**, e202315802 (2024).
29. Qin, J. et al. Altering ligand fields in single-atom sites through second-shell anion modulation boosts the oxygen reduction reaction. *J. Am. Chem. Soc.* **144**, 2197–2207 (2022).
30. Ni, B. et al. Second-shell N dopants regulate acidic O_2 reduction pathways on isolated Pt sites. *J. Am. Chem. Soc.* **146**, 11181–11192 (2024).
31. Xiao, M. et al. 3d-orbital occupancy regulated Ir-Co atomic pair toward superior bifunctional oxygen electrocatalysis. *ACS Catal.* **11**, 8837–8846 (2021).
32. Prabhu, P. et al. Subnanometric osmium clusters confined on palladium metallenes for enhanced hydrogen evolution and oxygen reduction catalysis. *ACS Nano* **18**, 9942–9957 (2024).
33. Tong, M. et al. Potential dominates structural recombination of single atom Mn sites for promoting oxygen reduction reaction. *Angew. Chem. Int. Ed.* **62**, e202314933 (2023).
34. Li, Z., Wang, S., Chin, W. S., Achenie, L. E. & Xin, H. High-throughput screening of bimetallic catalysts enabled by machine learning. *J. Mater. Chem. A* **5**, 24131–24138 (2017).
35. Ding, H. et al. Active learning accelerating to screen dual-metal-site catalysts for electrochemical carbon dioxide reduction reaction. *ACS Appl. Mater. Interfaces* **15**, 12986–12997 (2023).
36. Lundberg, S. M. et al. From local explanations to global understanding with explainable AI for trees. *Nat. Mach. Intell.* **2**, 56–67 (2020).
37. Chen, S. et al. Identification of the highly active Co-N_4 coordination motif for selective oxygen reduction to hydrogen peroxide. *J. Am. Chem. Soc.* **144**, 14505–14516 (2022).
38. Wang, M. et al. Atomically dispersed manganese on carbon substrate for aqueous and aprotic CO_2 electrochemical reduction. *Adv. Mater.* **35**, e2210658 (2023).
39. Kresse, G. & Furthmüller, J. Efficiency of ab-initio total energy calculations for metals and semiconductors using a plane-wave basis set. *Comput. Mater. Sci.* **6**, 15–50 (1996).
40. Perdew, J. P., Burke, K. & Ernzerhof, M. Generalized gradient approximation made simple. *Phys. Rev. Lett.* **77**, 3865–3868 (1996).
41. Blöchl, P. E. Projector augmented-wave method. *Phys. Rev. B Condens. Matter Mater. Phys.* **50**, 17953–17979 (1994).
42. Grimme, S. Semiempirical GGA-type density functional constructed with a long-range dispersion correction. *J. Comput. Chem.* **27**, 1787–1799 (2006).
43. Pedregosa, F. et al. Scikit-learn: Machine learning in python. *J. Mach. Learn. Res.* **12**, 2825–2830 (2011).
44. Yang, Y. The geometric-electronic coupled design of diatomic catalyst towards oxygen reduction reaction, YanYang233/ORR-ML:v1.0, https://doi.org/10.5281/zenodo.15300027 (2025).

Acknowledgements

This work was supported by the Natural Science Foundation of China (22303002, Y.L.; 22375006, J.M.) and the Anhui Provincial Natural Science Foundation (2408085MB035, Z.Z.). D.L. thanks the Fundamental Research Funds for the Central Universities (buctrc202007). Numerical computations were performed on Hefei Advanced Computing Center.

Author contributions

Y. Liu and J.J. conceived this work. Y.Y. proposed a Machine learning framework with guidance from Y. Liu, Z.Z. and J.J., Y.Y. performed DFT calculations and wrote the code with guidance from Y. Liu and Z.Z., X.L. and Y. Lin performed synthesis, characterization and performance tests with guidance from D.L. and J.M., Y. Liu, Y.Y. and X.L. analyzed the data and co-wrote the manuscript, with input from the other authors.

Competing interests

The authors declare no competing interests.

Additional information

Supplementary information The online version contains supplementary material available at https://doi.org/10.1038/s41467-025-60170-0.

Correspondence and requests for materials should be addressed to Zhiwen Zhuo, Dong Liu, Junjie Mao or Jun Jiang.

Peer review information *Nature Communications* thanks Wei Zhou, and the other, anonymous, reviewer(s) for their contribution to the peer review of this work. A peer review file is available.